Revisiting the Vertical-Axis Wind-Turbine Design using Advanced Computational Fluid Dynamics

John C. Vassberg [*]
Hydro-Aero Consulting Group
Long Beach, CA 90803, USA

Arathi K. Gopinath [†]
Stanford University
Stanford, CA 94305, USA

Antony Jameson [‡]
Stanford University
Stanford, CA 94305, USA

10 – 13 January, 2005

Abstract

The focus of the current work is to investigate the possibility of improving the efficiency of a vertical-axis wind-turbine design through application of emerging computational fluid dynamics capabilities under development at Stanford University. A three-dimensional spectral time-accurate CFD method has been extended to consider the dynamic motion of a turbine blade spinning about an axis and subjected to a farfield uniform freestream velocity flowfield. Parametric studies of turbine solidity (chord-to-radius ratio), turbine tip speeds, and a variation of a NACA0015 airfoil section are presented. Results are compared with experimental data for validation of the numerical method. Comparisons with windmill-class turbines are drawn to illustrate some possible operational benefits of the vertical-axis design.

Nomenclature

A_b	Planform Area of a Blade
A_s	Frontal Area Swept by Turbine
b	Blade Span
BDF	Backward Difference Formula
BET	Blade Element Theory
c	Chord Length of Blade Airfoil Section
CFD	Computational Fluid Dynamics
C_D	Total Drag Coefficient $= \frac{Drag}{q_\infty S_{ref}}$
C_L	Total Lift Coefficient $= \frac{Lift}{q_\infty S_{ref}}$
C_d	Sectional Drag Coefficient $= \frac{drag}{q_\infty C_{ref}}$
C_l	Sectional Lift Coefficient $= \frac{lift}{q_\infty C_{ref}}$
C_P	Pressure Coefficient $= \frac{P-P_\infty}{q_\infty}$
$C_\mathcal{P}$	Power Coefficient $= \frac{\mathcal{T}\omega}{q_\infty V_\infty A_s}$
h	Height Coordinate
$HAWT$	Horizontal-Axis Wind Turbine
N	Number of Spectral Modes
N_b	Number of Turbine Blades
$\mathcal{P}$	Power $= \mathcal{T}\omega = Tr\omega N_b$
q_∞	Freestream Dynamic Pressure $= \frac{1}{2}\rho V_\infty^2$
q_o	On-Set Dynamic Pressure $= \frac{1}{2}\rho V_o^2$
QST	Quasi-Steady Theory
$Q2D$	Quasi-Two-Dimensional Theory
r	Radial Coordinate
R	Max Turbine Radius; Flow Equation
$RANS$	Reynolds-Averaged Navier-Stokes
Re	Reynolds number based on Turbine Tip Speed
SOA	State of the Art
T	Thrust Per Blade; Time Period
$\mathcal{T}$	Torque $= TrN_b$
$\bar{V}_\infty$	Freestream Velocity Vector
$\bar{V}_b$	Blade Velocity Vector
$\bar{V}_o$	On-Set Velocity Vector $= \bar{V}_\infty - \bar{V}_b$
$VAWT$	Vertical-Axis Wind Turbine
x	Airfoil Chordwise Coordinate
y	Airfoil Thickwise Coordinate
w	Flow Variable
α	Angle of Attack
χ	Turbine Tip-Speed Ratio $= \frac{R\omega}{V_\infty}$
η	Non-Dimensional Semispan Coordinate
θ	Blade Angular Position
ω	Blade Angular Velocity
σ	Solidity $= \frac{N_b A_b}{A_s}$
∞	Infinity

1 Introduction

Harnassing the sustainable energy of the wind has been a quest of man for many centuries. In fact, there is something almost nostalgic about this pursuit, whether one is soaring thermals in a glider or simply flying a kite. But more importantly, the utilitarian benefits of extracting power from this universally available resource have been significant. These include the windmills of the old west used to pump water for cattle, sails to power ships for commerce

[*] AIAA Associate Fellow, Boeing Technical Fellow
[†] AIAA Member, Doctoral Candidate
[‡] AIAA Fellow, T. V. Jones Prof. of Engineering

and discovery, and now large-scale wind turbines capable of generating electricity for the masses. As the worldwide supply of fossil fuels dwindles, converting wind energy to electricity is becoming increasingly more important. Yet in addition to the huge turbines which typically populate wind farms, there is also a need to design small portable turbines which can be easily deployed in remote areas. The authors envision that the vertical-axis wind turbine (VAWT) will play a significant role in providing a solution for this requirement.

Figures 1-2 illustrate examples of H-Type and Darrieus vertical-axis wind-turbine designs, respectively. Note the orientation of the turbine's axis of rotation. Unlike typical windmills or horizontal-axis wind turbines (HAWT), the VAWT design operates independent of wind direction, and therefore does not require a weathervane. VAWTs can also be classified as drag-types or lifting-class turbines. The turbines of Figures 1-2 are of the lifting class. An example of a drag-type turbine is an anemometer, where the torque generated is the result of the "blade" having a much higher drag coefficient with a tail wind than it does when advancing into the flow. By observation, the tip speed of a drag-type VAWT cannot exceed the velocity of the freestream wind. The discussions in the remainder of this paper concentrate on the lifting-class turbine design.

Relative to HAWT designs, the power-extraction efficiency of existing VAWT designs have fallen short. In the literature, the accepted understanding for this shortcoming is that the power output of a VAWT blade is cyclic during a revolution while that of a HAWT blade is essentially constant. This fundamental difference in operation has certainly made it easier for designers to optimize the performance of the HAWT. In addition, it seems likely that a design with a constant optimum output should have the advantage over a design with a cyclic power generation that only passes through optimal states a couple of times per revolution. In principal however, this may not necessarily be the case.

There was much research during the 1970's and early 1980's to investigate the feasibilities of various wind-turbine concepts. During this period, the state-of-the-art (SOA) of aerodynamic methods for the analysis of these turbines was based on quasi-2D and quasi-steady calculations.

Blade element theory (BET) has been the basis of HAWT designs for decades. BET can be traced back a century to the propellor design work of the Wright brothers. The levels of efficiency that they attained in their propellor designs is evidence that this quasi-two-dimensional analysis technique provides a fairly accurate representation of the performance characteristics of a three-dimensional propellor system. In BET, the 3D problem is studied by individually analyzing the performance of a number of airfoil sections across the span of the propellor blade, then integrating these results to yield a close approximation to the performance of the complete propellor. Typically, the aerodynamic performance of the airfoil sections is known through wind-tunnel experimentation. The HAWT design work of the 1970's exploited BET and yielded fairly close to optimum wind turbines. Conversly, the aerodynamic analysis methods for VAWT configurations were not so well developed.

The SOA for VAWT analysis during the 1970's was based on quasi-steady theory (QST). The underlying assumption of QST is that the instantaneous forces acting on a dynamically rotating blade are equivalent to those acting on the static blade under the same instantaneous on-set flow conditions. This assumption is quite appropriate in the limit as the reduced frequency approaches zero. This occurs when either the solidity or the tip-speed ratio approaches zero. However, under the normal operating conditions of a lifting-class VAWT, this introduces significant error in the analysis technique because the hysteresis of a pitching airfoil can be quite large. Here, the instantaneous on-set flow conditions are based purely on a geometric reconstruction of the farfield velocity vector acting on the velocity vector of the advancing airfoil.

Figure 3 provides a two-dimensional schematic drawing of a VAWT cross-section to illustrate how the lifting-class turbine works. It also defines some nomenclature that has been adopted in this work. The clock position of a blade, θ, starts at zero where the blade velocity is directly opposing the freestream flow, and increases in a counter-clockwise direction. The angular velocity of the turbine is defined by the parameter ω. The turbine blade speed is described by a non-dimensional parameter which is defined as the ratio of its maximum blade speed normalized by the freestream wind velocity,

$$\chi \equiv \left[\frac{V_b}{V_\infty}\right] = \left[\frac{R\omega}{V_\infty}\right]$$

where R is the maximum radius of the turbine. Refering back to Figure 3, note that the on-set velocity vector is the difference between the freestream flow and the blade motion, $\bar{V}_o = \bar{V}_\infty - \bar{V}_b$. The angle between the on-set and blade velocity vectors is the instantaneous angle-of-attack, α. The lift & drag generated by the airfoil, respectively, act perpendicular & parallel to the on-set velocity. Depending on clock position and the L/D performance characteristics of the blade, the resultant force $(\bar{L} + \bar{D})$ can have a thrust component, $\bar{T}$, that acts in the positive θ direction, thus yielding a positive torque, $\mathcal{T}$, driving the system to generate power, $\mathcal{P} = \mathcal{T}\omega$.

In practice, the thrust vector cycles between slightly negative values near $\theta = 0°$ & $180°$, and local maxima near $\theta = 90°$ & $270°$. Integration over the full 360 degrees of motion provides an average positive result. The maximum power output typically occurs with tip speeds in the range $3 \leq \chi \leq 8$.

For an H-Type turbine, the general geometric properties of the cross-section depicted in Figure 3 are usually constant with varying span station. However in the case of a Darrieus design, these geometric properties vary with the local radius. Hence, the non-dimensional speed of the local blade section also varies as

$$\chi_s = \chi \left[\frac{r_s(h)}{R} \right] \tag{1}$$

where r_s is the radius of local blade section sweep, h is the height coordinate of the turbine cross-section, and R is the maximum radius of the turbine sweep. Another geometric property of a VAWT is that it is symmetric vertically about the mid-span station, i.e., at $h = b/2$, where b is the vertical span of the turbine blades. Because of this property, another non-dimensional parameter used herein is the semi-span location as defined by

$$\eta(h) = \frac{h - (b/2)}{(b/2)}, \quad \left[\frac{b}{2}\right] \leq h \leq b.$$

Note that the on-set angle-of-attack for the airfoil swings through a full 360-degree motion if the turbine tip speed is less than the magnitude of the farfield velocity. However, if the turbine tip speed is greater than that of the farfield velocity, the range of angle-of-attack that the airfoil experiences is reduced with increasing tip speed. This effect is illustrated in Figure 4. The maximum angle-of-attack can be determined to be $\alpha_{max} = atan(1/\chi)$. For example, consider a turbine tip speed of $\chi = 3.0$. In this case, the maximum angle-of-attack that the airfoil is subjected to is $\alpha_{max} = 18.4°$.

Consider a turbine blade based on the NACA0015 airfoil section. Figures 5-6 provide wind-tunnel data for this airfoil at a Reynolds number typical of VAWT operating conditions. Since the NACA0015 is a symmetric airfoil, this data spans the full 360° of motion, necessary for turbine tip speeds of $\chi \leq 1$. The need for this full range of alpha data is associated with the start-up phase. When there has been a period of calm, such as at night, any wind turbine naturally comes to rest. When the farfield wind velocity begins to rise, it is imperative that a wind turbine be able to self start. Figure 7 illustrates the thrust generated by a single-blade NACA0015 airfoil as a function of clock position. If the thrust coefficient is negative, the turbine will begin to spin backwards until it reaches a clock position where the thrust changes sign. In this mode, the turbine will eventually come to rest at a stable position and remain there, no matter how fast the farfield wind velocity becomes. This is clearly the case for a single-blade starting in positions in the range of $20° \leq \theta \leq 90°$ and $160° \leq \theta \leq 180°$. Referring to Figure 8, one can see that this design will self start if six evenly spaced blades are utilized. Although, considering the normal small fluctuations in wind direction, it appears that a five-blade design will more than likely self start as well.

2 Mathematical Formulation

This section describes the mathematical formulation of the fundamental algorithms of UFLO107. This numerical method is utilized in this work to compute the time-accurate three-dimensional viscous flows about vertical-axis wind turbines.

Governing Equations

The Navier-Stokes equations in integral form are given by

$$\int_\Omega \frac{\partial w}{\partial t}\, dV + \oint_{\partial\Omega} \vec{F} \cdot \vec{N}\, ds = 0.$$

In semi-discrete form, the unsteady equations in Cartesian coordinates can be written as

$$V \frac{\partial w}{\partial t} + R(w) = 0, \qquad R(w) = \frac{\partial}{\partial x_i} f_i(w), \tag{2}$$

where w is the vector of conserved variables,

$$w = \begin{bmatrix} \rho \\ \rho u_1 \\ \rho u_2 \\ \rho u_3 \\ \rho E \end{bmatrix}$$

and $R(w)$ is the residual vector of spatial discretization representing contributions from both the physical inviscid and viscous fluxes and numerical dissipation fluxes.

If the mesh is moving with velocity components u_{1m}, u_{2m} and u_{3m} at each mesh point, the fluxes f_i are given by

$$f_i = f_{ci} - f_{vi},$$

where the convective fluxes f_{ci} and viscous fluxes f_{vi} are defined as

$$f_{ci} = \begin{bmatrix} \rho u_{ir} \\ \rho u_{ir} u_1 + p\delta_{i1} \\ \rho u_{ir} u_2 + p\delta_{i2} \\ \rho u_{ir} u_3 + p\delta_{i3} \\ \rho u_{ir} H \end{bmatrix},$$

$$f_{vi} = \begin{bmatrix} 0 \\ \tau_{i1} \\ \tau_{i2} \\ \tau_{i3} \\ \vec{u} \cdot \vec{\tau_i} - q_i \end{bmatrix},$$

here $u_{ir} = u_i - u_{im}$ and δ is the Kronecker delta. $\bar{\bar{\tau}}$ is the stress tensor and its components are given by,

$$\tau_{ii} = 2\mu u_i + \lambda(u_{1,x_1} + u_{2,x_2} + u_{3,x_3}),$$

$$\tau_{ij} = \tau_{ji} = \mu(u_{i,x_j} + u_{j,x_i}),$$

here $\lambda = \frac{-2}{3}\mu$ and the heat flux vector q's components are given by

$$q_i = -\kappa T_i.$$

T_i are temperature gradients and

$$\kappa = \gamma(\frac{\mu_{lam}}{Pr_{lam}} + \frac{\mu_{turb}}{Pr_{turb}}).$$

μ_{lam} and μ_{turb} are the laminar and turbulent kinematic viscosities, Pr_{lam} and Pr_{turb} are the laminar and turbulent Prandtl numbers.

The equation of state provides the closure. For ideal gas,

$$p = (\gamma - 1)\rho(E - \frac{u_{ii}}{2})$$

and

$$H = E + \frac{p}{\rho}.$$

In this work, turbulent flow is modeled by the Reynolds-Averaged Navier-Stokes (RANS) equations with a turbulence model.

Backward-Difference Formula

In order to solve the unsteady governing equations time-accurately, the Backward Difference Formula discretizes Eqn (2) implicitly as

$$D_t(V^{n+1}w^{n+1}) + R(w^{n+1}) = 0.$$

The operator D_t of k^{th} order accuracy is of the form

$$D_t = \frac{1}{\Delta t}\sum_{q=1}^{k}\frac{1}{q}(\Delta^-)^q,$$

where

$$\Delta^- w^{n+1} = w^{n+1} - w^n.$$

For example, the second-order A-stable BDF scheme is

$$\frac{3w^{n+1}V^{n+1} - 4w^nV^n + w^{n-1}V^{n-1}}{2\Delta t} + R(w^{n+1}) = 0,$$

where Δt is the physical time step. Since we have a rigidly-moving body-fitted mesh, $V^{n+1} = V^n = V^{n-1} = V$. Then,

$$V\frac{3w^{n+1} - 4w^n + w^{n-1}}{2\Delta t} + R(w^{n+1}) = 0.$$

Dual Time Scheme

Jameson [1] proposed the multigrid dual time stepping BDF that consists of the coupled non-linear equations, and solved them by inner iterations which advance in pseudo-time t^* to steady-state. Hence the scheme solves

$$\frac{\partial w}{\partial t^*} + R^*(w) = 0,$$

where

$$R^*(w) = V\frac{3w^{n+1} - 4w^n + w^{n-1}}{2\Delta t} + R(w^{n+1}).$$

An explicit multistage Runge-Kutta time-marching scheme with variable local Δt^* along with multigrid and residual averaging is implemented. If a large number of inner iterations are required at each physical time step, then the method becomes very expensive and calls for a better algorithm for the inner iterations.

Time-Spectral Methods

In the case of the vertical-axis wind turbine, the unsteady flow is time periodic. Taking advantage of the periodic nature of the problem, a Fourier representation in time can make it possible to achieve spectral accuracy. Also, if engineering accuracy can be obtained with small number of modes, then dramatic reductions in computational time can be achieved.

Recall the semi-discrete form of the governing equations (2),

$$V\frac{\partial w}{\partial t} + R(w) = 0.$$

The discrete Fourier transform of w is given by

$$\hat{w}_k = \frac{1}{N}\sum_{n=0}^{N-1} w^n e^{-ik\frac{2\pi}{T}n\Delta t}$$

and its inverse transform,

$$w^n = \sum_{k=-\frac{N}{2}}^{\frac{N}{2}-1} \hat{w}_k e^{ik\frac{2\pi}{T}n\Delta t}, \qquad (3)$$

where the time period T is divided into N time steps, $\Delta t = T/N$.

Discretize the governing equations as a pseudo-spectral scheme,

$$VD_t w^n + R(w^n) = 0. \qquad (4)$$

McMullen et.al. [2, 3] solved the time accurate equations in (4) by transforming them into a frequency

domain and introducing a pseudo-time t^*, like in the case of the dual time stepping scheme,

$$V\frac{\partial \hat{w}_k}{\partial t^*} + V\frac{2\pi}{T}ik\hat{w}_k + \hat{R}_k = 0.$$

Alternatively, the Time-Spectral Algorithm proposes to solve the governing equations in the time-domain, considerably gaining on the computational time required to transform back and forth to the frequency domain.

From Eqn (3), the time discretization operator D_t can be written as

$$D_t w^n = \frac{2\pi}{T}\sum_{k=-\frac{N}{2}}^{\frac{N}{2}-1} ik\hat{w}_k e^{ikn\Delta t}.$$

This summation involving the Fourier modes $\hat{w}_k$, can be rewritten in terms of the conservative variables w in the time domain as

$$D_t w^n = \sum_{m=-\frac{N}{2}+1}^{\frac{N}{2}-1} d_m w^{n+m},$$

where

$$d_m = \begin{cases} \frac{2\pi}{T}\frac{1}{2}(-1)^{m+1}cot(\frac{\pi m}{N}) & : \quad m \neq 0 \\ 0 & : \quad m = 0 \end{cases}$$

Note that $d_{-m} = -d_m$. The operator D_t hence is a central difference operator connecting all the time levels, so yielding an integrated space-time formulation which requires the simultaneous solution of the equations for all time levels.

A pseudo-time t^* is introduced like in the dual time stepping case, and the equations are time marched to a periodic steady-state

$$V\frac{\partial w^n}{\partial t^*} + VD_t w^n + R(w^n) = 0.$$

A 5-stage Runge-Kutta scheme is used to solve the equations in pseudo-time, and convergence to steady-state is accelerated by a multigrid procedure. Eddy-viscosity for the RANS equations is modeled with Baldwin-Lomax turbulence model.

Details of the numerical implementation and validation of the scheme are presented in a companion paper [4]. For completeness, we show a validation test case for a representative two-dimensional problem.

Validation using AGARD CT6

A well documented test case is provided by the AGARD CT6. This case is a NACA64A010 airfoil which is forced through an oscillatory pitching motion. Table 1 summarizes the characteristics of this experimental test conducted by Davis [5].

M_∞	α_m, $deg.$	Re_c, $(million)$	α_0, $deg.$	k_c
0.796	0.0	12.56	1.01	0.202

Table 1: Parameters of AGARD CT6

In order to validate the present time-spectral method, the turbulent Navier-Stokes equations are solved on a 256x64 C-mesh. The near-field resolution of this mesh is shown in Figure 9. These solutions are computed with 4, 8 & 12 intervals in the time period of oscillation of the pitching airfoil, corresponding to 2, 4 & 6 temporal modes (i.e., the steady state plus 1, 3 & 5 harmonics). Coefficient of lift (C_l) as a function of angle of attack is provided in Figure 10. Note that the numerical simulations compare closely with the experimental data. Furthermore, a temporal-mode convergence is achieved as is evidenced by the minor deviation of the lift-alpha loop with the variation in temporal resolution.

3 Turbine Geometries

The three-dimensional unsteady simulations presented in the following sections are performed on three different turbine configurations. In all three cases, our investigations have been conducted on single-blade designs.

The first and second turbines are H-Type configurations, with one based on the NACA0015 airfoil, and the other based on a modified version of this section. The modified airfoil, designated WARP0015-RC8, is a NACA0015 that has been warped such that the camber line coincides with the circular arc path of a turbine blade with a radius-to-chord ratio of 8.0, see Figure 11. Note that the y coordinates in this figure have been amplified to emphasize the difference between the airfoils. These airfoil sections are applied to a rectangular blade with a span-to-chord ratio of 5.0.

The third is a Darrieus-class turbine which is 17 meters high with a blade sweep diameter, also of 17 meters. The blade sections are NACA0015 airfoils with a chord length of 0.61 meters. The "dihedral" shape of a Darrieus turbine blade is that of a troposkien curve. (Troposkien is Greek meaning "turning rope", see Reference [6].) Similar to the classic catenary, a troposkien is defined as the equilibrium shape of a rope or cable subjected to a transverse acceleration. In the case of the catenary, gravity imposes a constant acceleration on the rope. For the troposkien, a centrifugal acceleration drives the shape. This acceleration varies along the length of

the rope and is directly proportional to the radial distance from the axis of rotation. The corresponding troposkien shape has been numerically computed such that the maximum diameter of the blade sweeping path is equivalent to the turbine height. Figure 12 provides this troposkien with a comparison to a catenary curve for reference. The desirable property of these shapes is that their internal loads are aligned with the curve. Hence, the structure is only subjected to pure tensile stresses; no bending stresses. This property is exploited in Darrieus designs to minimize the weight of the turbine, usually to reduce manufacturing costs. However it can also be a positive attribute when portability is a primary design consideration.

4 Results

This section presents numerous UFLO107 results on the three geometries described previously in § 3. To help orient the reader, an initial discussion is provided in the context of a two-dimensional quasi-steady analysis. This review also illustrates the shortcomings of this analysis technique. Additional studies are provided which show the effect of an airfoil change, illustrate the effect of solidity, and back-solve for sectional characteristics from a database of turbine power coefficients.

Quasi-Steady Analysis using FLO103

To accurately discriminate the differences between a quasi-steady analysis and the Time-Spectral RANS CFD method, a database of steady-state aerodynamic characteristics is generated for the NACA0015 airfoil using FLO103. FLO103 and the Time-Spectral method of UFLO107 are based on the same fundamental algorithms, however, FLO103 is a two-dimensional flow solver.

Figures 13-14 depict the FLO103 results for the NACA0015 airfoil over an angle-of-attack range of $-16^\circ \leq \alpha \leq 16^\circ$, with freestream conditions of $M = 0.3$ and $Re = 2M$, and using the Baldwin-Lomax turbulence model. This database has been curve-fit for the convenience of data extraction and is described by the following set of equations.

$$\begin{aligned} C_l(\alpha) &\doteq 0.11869\alpha - 0.0000449\alpha^3 \\ C_d(C_l) &\doteq 0.0039 + 0.004C_l^2 \\ &\quad +0.0006C_l^4 + 0.00006C_l^8 \end{aligned} \tag{5}$$

where the units of α are in degrees.

The turbine condition that is emphasized in this discussion has a blade speed ratio of $\chi = 5.0$, and a radius-to-chord ratio of 8.0 (solidity of $\sigma = 0.0625$). Figure 15 depicts the geometric angle-of-attack as a function of blade position for this condition. Note that the maximum angle-of-attack falls well within the database range of Eqn (5). Since all coefficients are referenced by the freestream dynamic pressure, yet the spinning blade is subjected to a higher on-set flow velocity, the coefficients of Eqn (5), using $\alpha(\theta)$ of Figure 15, must be scaled by the dynamic pressure ratio of the on-set flow, which is provided in Figure 16. This gives the sectional lift cycle depicted in Figure 17. Cross plotting Figures 15 & 17 yields the infinity-shaped lift loop of Figure 18. Although the C_l-α curve of Figure 13 is single valued, the dynamic lift loop exhibits a hysteresis due to the fact that the on-set dynamic pressure varies during the periodic cycle. Further examination of the lift loop shows that as the blade advances forward from $\theta = 0^\circ$, both lift & α are negative and reside on the negative extreme branch of the lift loop. As the blade passes through $\theta = 90^\circ$ and begins to retreat down-wind, the lift increases rapidly at first, then steadily, then rapidly again as the blade approaches $\theta = 270^\circ$, where it begins its advancement back into the freestream wind.

In order to compute the power cycle, the above process is repeated for the drag loop, then these forces are transformed into the thrust coefficient aligned with the θ direction.

$$C_t(\theta) = C_l \; sin(\alpha) - C_d \; cos(\alpha) \tag{6}$$

Here C_l, C_d and α are all functions of θ. The power coefficient is defined as

$$\begin{aligned} C_{\mathcal{P}} &\equiv \frac{\mathcal{T}\omega}{\frac{1}{2}\rho V_\infty^3 A_s} \\ &= \frac{TR\omega N_b}{q_\infty V_\infty 2Rb} \\ &= \left[\frac{T}{q_\infty cb}\right]\left[\frac{V_b}{V_\infty}\right]\left[\frac{N_b\, c}{2R}\right] \\ &= C_t \; \chi \; \sigma \end{aligned} \tag{7}$$

where ω is the rotational velocity, $\sigma = (N_b\, c)/(2R)$ is the solidity parameter, N_b is the number of blades, c their chord length, and R is the radius of their rotation. Note that the denominator on the right-hand-side of the first line in Eqn (7) is the total available freestream wind energy that passes through an area equivalent to that swept by the turbine. For reference, the Betz limit for a windmill-class HAWT is $C_{\mathcal{P}\,BETZ} \simeq 0.59$.

NACA0015 vs. WARP0015-RC8

An investigation is conducted to determine the effect of modifying the NACA0015 airfoil as described in

§ 3. In addition, the discussion of the previous section continues into this section with comparisons of the results.

The 3D simulations of the H-Type VAWT are conducted on a C-mesh of dimension (192x64x24) cells, using 8 time intervals, with conditions $M_\infty = 0.1$, $\chi = 5.0$, and $Re = 1M$. The resulting time-averaged power coefficients for the 3D systems are

$$\begin{aligned} C_{\mathcal{P}\,NACA} &= 0.3117 \\ C_{\mathcal{P}\,WARP} &= 0.3238 \end{aligned}$$

showing a marginal improvement of $\simeq 4\%$ for the modified airfoil. (Note: In addition to the thrust-related torque, the power coefficient computed by UFLO107 includes contribution of the dynamic moment acting on the blade.)

Since the quasi-steady analysis is fundamentally a two-dimensional evaluation, the corresponding comparisons are made with respect to the mid-blade-station sectional properties extracted from the three-dimensional Time-Spectral flow solutions.

Figures 19-22 provide detailed sectional data at the mid-blade station (i.e., at $\eta = 0$). Figure 19 compares the sectional lift loops of the quasi-steady analysis with those of the Time-Spectral simulations for both the NACA0015 and the WARP0015-RC8 turbines. Figure 20 provides a similar comparison of the drag-polar loops. From these figures, it is obvious that the quasi-steady analysis significantly over predicts the aerodynamic performance of the turbine. This observation is confirmed with the cyclic power comparison of Figure 21.

The mid-blade-station pressure distributions for the WARP0015-RC8 turbine are given in Figure 22 at $\theta = [0, 90, 180, 270]$ degrees. Note that the pressures for $\theta = 90°$ & $270°$ are almost identical, with the pressure peak occuring on the down-wind side of the blade. While not provided here, a similar plot for the NACA0015 pressures shows a negative-cambering effect which hyper-loads the blade from $0° \leq \theta \leq 180°$ and unloads it from $180° \leq \theta \leq 360°$.

Figure 23 illustrates the computed spanwise variation of the time-averaged sectional power coefficients for both geometries; both solutions show very similar spanload trends. This figure also shows that the peak power is being generated at the mid-span station ($\eta = 0$) and that the tip effect near $\eta = 1$ is detrimental to the overall power output of these H-Type turbines. Addressing the issue of losses at the blade tip should dramatically improve the efficiency of future VAWT designs, with the potential of achieving a total power coefficient approaching $C_\mathcal{P} \simeq 0.5$, as indicated by what is achieved at the mid-span station of the above results.

Effect of Solidity

The effect of solidity on power generation is studied for the NACA0015 H-Type turbine. Figure 24 gives this trend for a fixed tip speed of $\chi = 5.0$. In this example, the maximum power output occurs at $\sigma = 0.8\bar{3}$ or at a chord-to-radius ratio of 6.0. Deviating σ in either direction reduces the power in an almost symmetric manner. For $\sigma \geq 0.17$, the power coefficient is negative.

Darrieus 17M Turbine

The final case studies are conducted on a 17-meter Darrieus-class turbine, similar to one that has been experimentally investigated by the Sandia National Laboratories in Albuquerque, New Mexico. See References [7, 8]. The primary difference between the present geometry under study and Sandia's is the number of blades; a secondary difference is in the thickness of the airfoil sections. Figure 25 provides a comparison of computed *vs* experimental power trends as a function of tip speed. It is encouraging that these curves have similar shape, are almost identical at low values of χ, and exhibit a shift in peak location/value that shows a trend with varying blade count. However, it appears that the computed power coefficient trend remains somewhat optomistic at the higher values of χ relative to the experimental data, even after taking into consideration the trend associated with the number of blades.

The computed spanwise variation of the sectional power coefficients for the $\chi = 5.0$ condition is shown in Figure 26. Compare this result with those for the H-Type turbines of Figure 23. It is interesting to note that while the Darrieus spanload exhibits a less adverse tip effect than that associated with the H-Type configurations, it is more triangular in shape, and therefore does not achieve the same level of performance.

Since the local sectional blade speed varies along the span of a Darrieus turbine, an exercise was conducted to try to reverse-engineer the sectional power coefficient function from Sandia's experimental data. This study was performed prior to having the ability to directly compute this information with UFLO107. The intention is to determine just how high the sectional power coefficient of the Sandia data might reach, thereby providing additional insight to what power-coefficient level might be attainable. In order to facilitate this exercise, an assumption is made that the sectional power coefficient is strictly a function of local section blade speed. We then seek a function, $C_{\mathcal{P}s}(\chi_s)$, that when integrated over the span of the blade yields the function $C_\mathcal{P}(\chi)$. Here, the subscript s designates local sectional quantities. This gives the

following equation to be solved.

$$C_{\mathcal{P}}(\chi) = \frac{1}{A_s} \int_0^b r_s(h)\, C_{\mathcal{P}s}(\chi_s)\, dh, \quad \forall\, \chi \qquad (8)$$

where b is the span of the blade, h is the height coordinate, r_s is the local sectional radius defined by the troposkien curve of Figure 12, χ_s is the section blade speed defined in Eqn (1), R is the maximum turbine radius, and A_s is the frontal area swept by the turbine. Examination of Eqn (8) reveals that this system is triangular in nature as $\chi_s \leq \chi$ for all values of χ. Inverting a discrete form of Eqn (8) for $\chi \leq 6.0$ yields the piecewise-linear $C_{\mathcal{P}s}(\chi_s)$ function shown in Figure 27. This figure also provides the result of substituting $C_{\mathcal{P}s}(\chi_s)$ back into Eqn (8) to verify that an accurate representation of the original test data is recovered.

Figure 28 provides a comparison of the $C_{\mathcal{P}s}(\chi_s)$ function with results from the Time-Spectral method. Here, the computed data is identical to that of Figure 26, but now plotted against local section blade speed, χ_s. It can be seen that there is a substantial discrepancy between the reverse-engineered trend and that of the direct numerical simulation for this case. Thus, it appears that our original assumption that $C_{\mathcal{P}s}$ is strictly a function of χ_s was not correct. In retrospect, and with the benefit of numerical results such as those shown in Figures 23 & 24, it is now obvious that the sectional power coefficient is also influenced by three-dimensional effects, solidity and Reynolds number.

5 Conclusions

This work represents a first attempt by the authors to introduce a high-fidelity numerical model for the simulation of the three-dimensional unsteady, periodic, viscous flows associated with vertical-axis wind turbines. The numerical method utilized, UFLO107, is based on a spectral discretization of the RANS equations in the time domain.

Parametric variations of turbine tip speeds, solidity, and airfoil sections are investigated, culminating with numerical studies in which over 25 time-accurate three-dimensional RANS CFD solutions were performed. So far, the calculations have been restricted to single-blade turbines. While the computed trends show some resemblance to experimental data, it will be essential to conduct numerical simulations on multi-blade configurations to gain better insight into this intriguing aerodynamic problem. Nonetheless, the investigations conducted thus far indicate that there are items to be addressed that can potentially improve the efficiency of future vertical-axis wind-turbine designs.

Post Script

It is well known that the influence of the helical wake in helicopter-rotor flows has a significant impact on the aerodynamic performance of the rotor. Therefore is it reasonable to expect that the trailing wakes of a VAWT also have a significant influence on their power-generating capabilities, maybe even more so since the wakes from the upstream VAWT-blades are pierced by blades passing through the downstream half-space of the turbine swing. The present work did not include a detailed study to understand how best to resolve the trailing wakes as they convect downstream. In order to carry out such a study, the size of the grid dimension will probably increase by an order-of-magnitude.

In addition, a set of grid-resolution studies should be conducted to determine what requirements are needed to sufficiently capture the unsteady vortex-shedding that occurs at the blade tips as well as near the blade trailing edge. While this will undoubtedly further increase the dimension of the grid, the authors believe that these investigations are required before very-accurate simulations of the VAWT flow-field can be achieved.

The studies performed thus far have been accomplished without the benefit of any direct funding. In order to pursue the outstanding issues in further detail, some level of additional funding may be required.

Acknowledgments

The first author thanks The Boeing Company for allowing his participation in this project. The development of the time-spectral method has benefited from the generous support of the Department of Energy under contract number LLNL B341491 as part of the Accelerated Strategic Computing Initiative (ASCI) program at Stanford University.

References

[1] A. Jameson. Time dependent calculations using multigrid, with applications to unsteady flows past airfoils and wings. (91-1596), June 1998.

[2] M. McMullen, A. Jameson, and J.J. Alonso. Acceleration of convergence to a periodic steady state in turbomachinery flows. *AIAA paper 01-0152*, AIAA 39th Aerospace Sciences Meeting, Reno, NV, January 2001.

[3] M. McMullen, A. Jameson, and J.J. Alonso. Application of a non-linear frequency domain solver to the euler and navier-stokes equations. *AIAA*

paper 02-0120, AIAA 40th Aerospace Sciences Meeting and Exhibit, Reno, NV, January 2002.

[4] A. Gopinath and A. Jameson. Time spectral method for periodic unsteady computations over two- and three- dimensional bodies. *AIAA paper 05-1220*, 43rd AIAA Aerospace Sciences Meeting and Exhibit, Reno, NV, January 10-13 2005.

[5] S.S. Davis. Naca 64a010 (nasa ames model) oscillatory pitching. *AGARD Report 702*, January 1982.

[6] B.F. Blackwell and G.E. Reis. Blade shapes for a troposkien type of vertical-axis wind turbine. *Report SLA-74-0154*, Sandia Laboratories, Albuquerque, NM, April 1974.

[7] M.H. Worstell. Aerodynamic performance of the 17-meter diameter darrieus wind turbine. *Report SAND78-1737*, Sandia Laboratories, Albuquerque, NM, September 1978.

[8] M.H. Worstell. Aerodynamic performance of the 17-m-diameter darrieus wind turbine in the three-bladed configuration: An addendum. *Report SAND79-1753*, Sandia Laboratories, Albuquerque, NM, 1979.

Figure 1: A 5-Blade H-Type Vertical-Axis Wind Turbine.

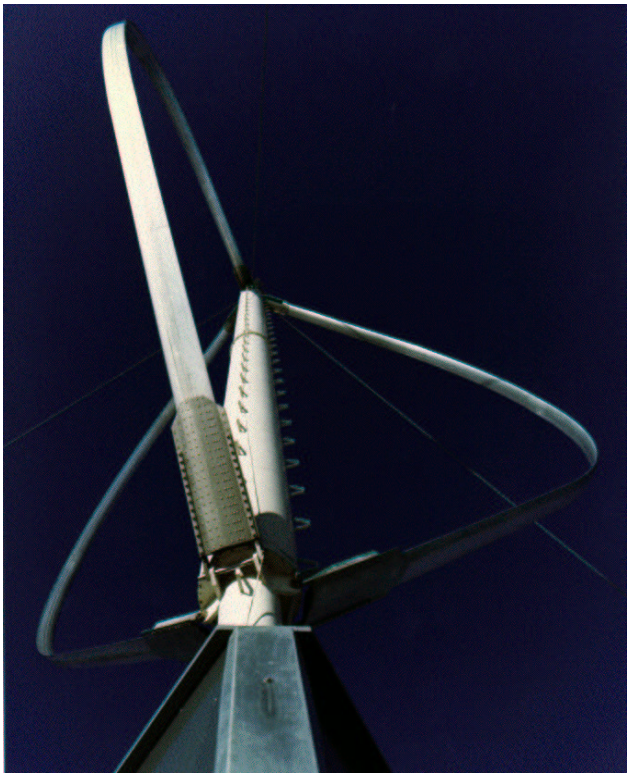

Figure 2: A 3-Blade Darrieus Vertical-Axis Wind Turbine.

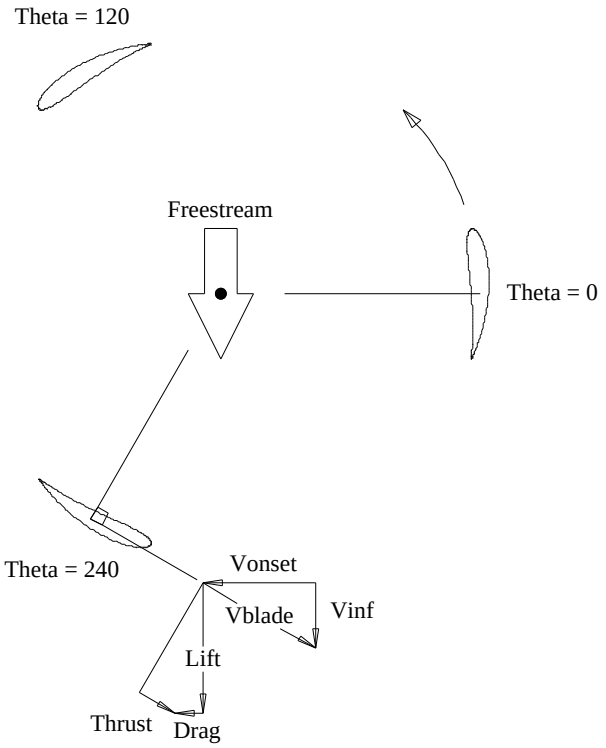

Figure 3: Schematic of a Vertical-Axis Wind Turbine Cross-Section.

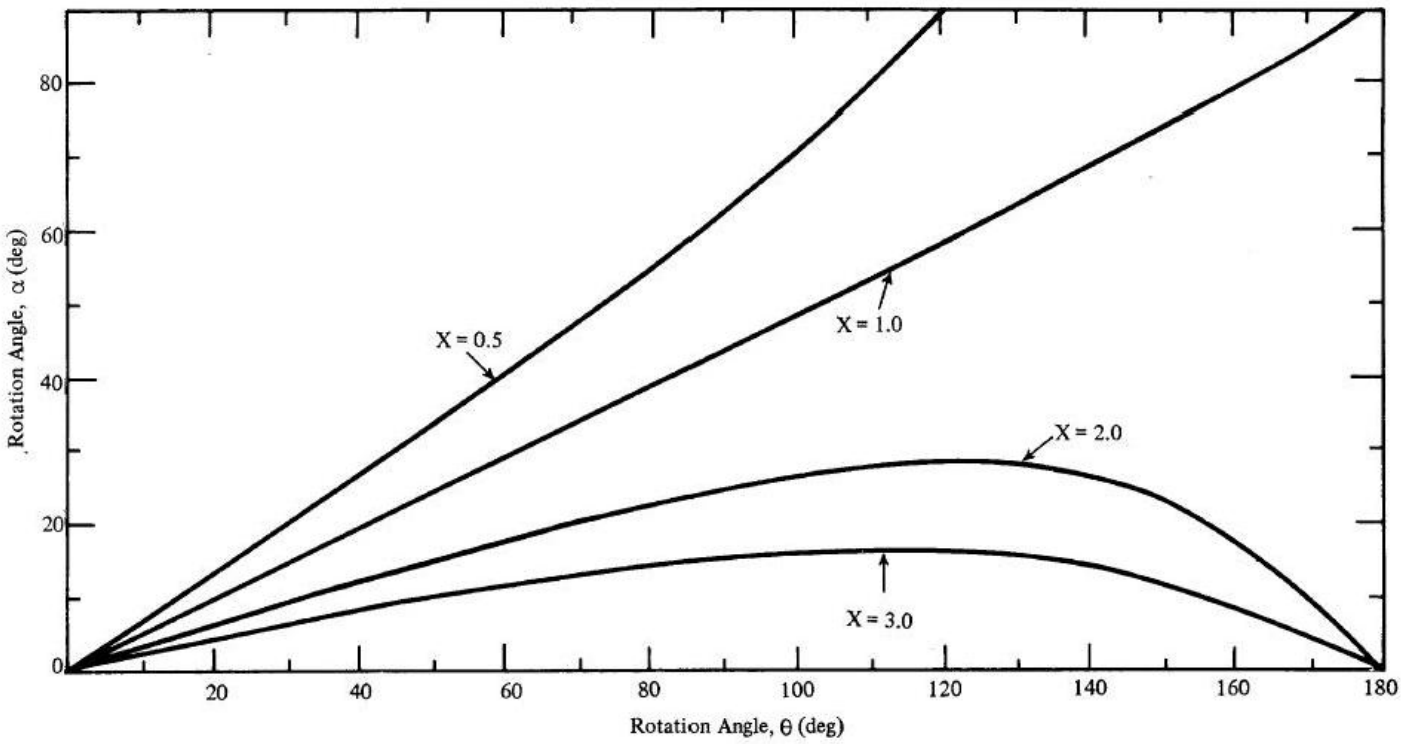

Figure 4: Effect of Turbine Tip Speed on Angle-of-Attack Range.

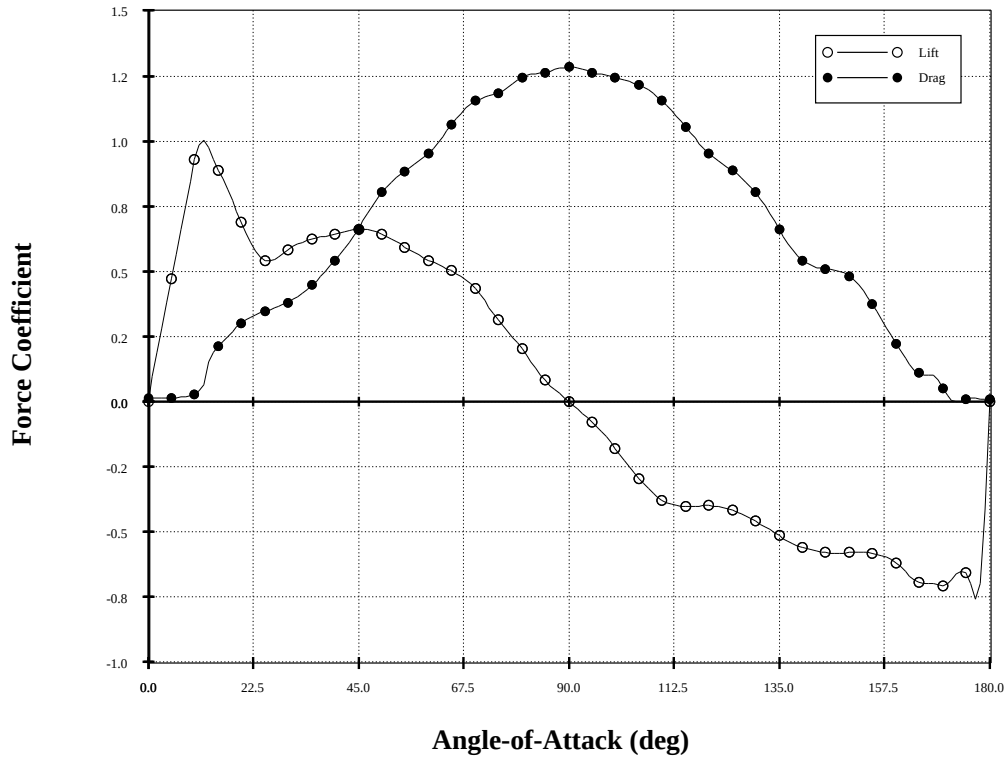

Figure 5: NACA0015 Experimental Lift & Drag Coefficients - Full Alpha Sweep.

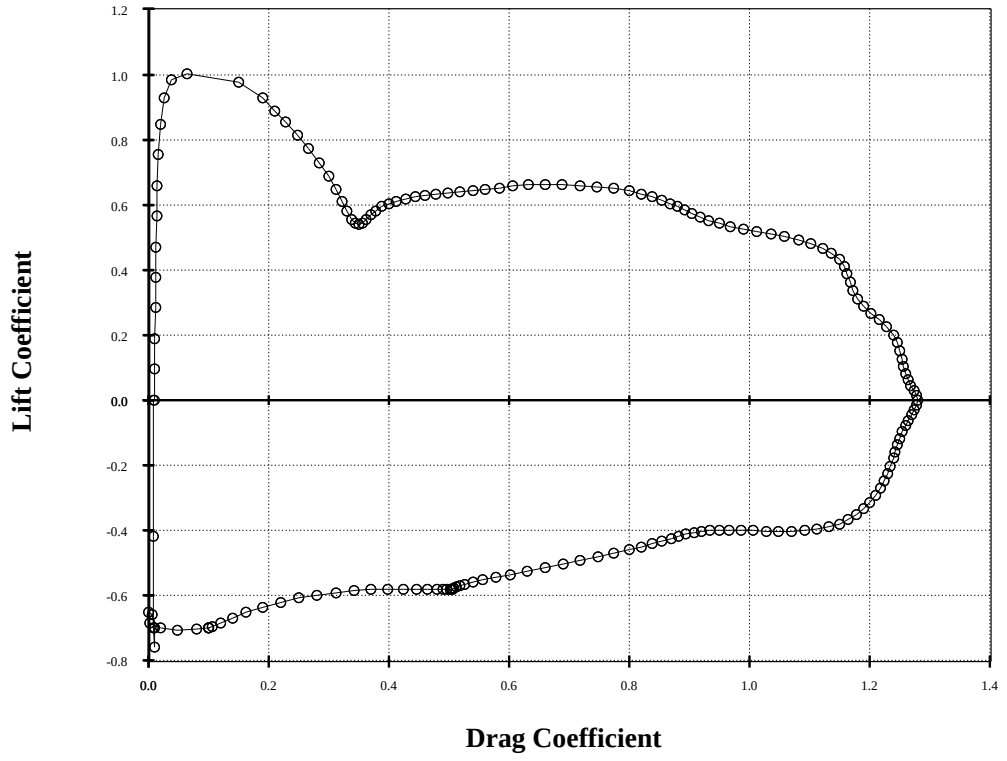

Figure 6: NACA0015 Experimental Drag Polar - Full Alpha Sweep.

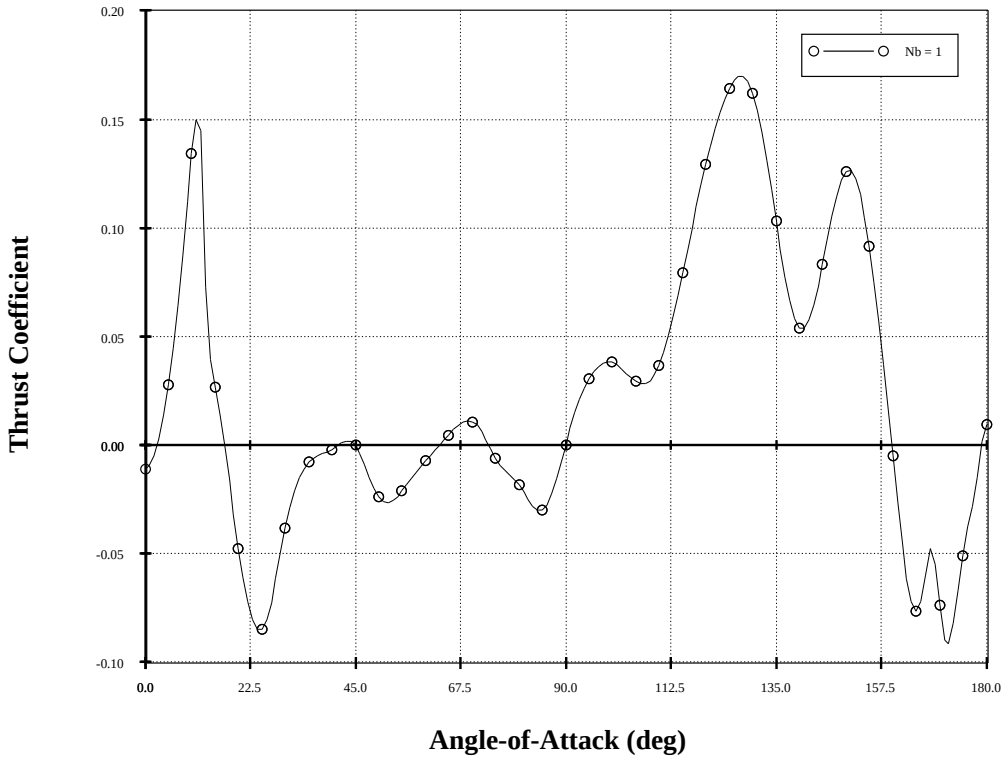

Figure 7: NACA0015 Thrust Coefficient Derived from Experimental Data.

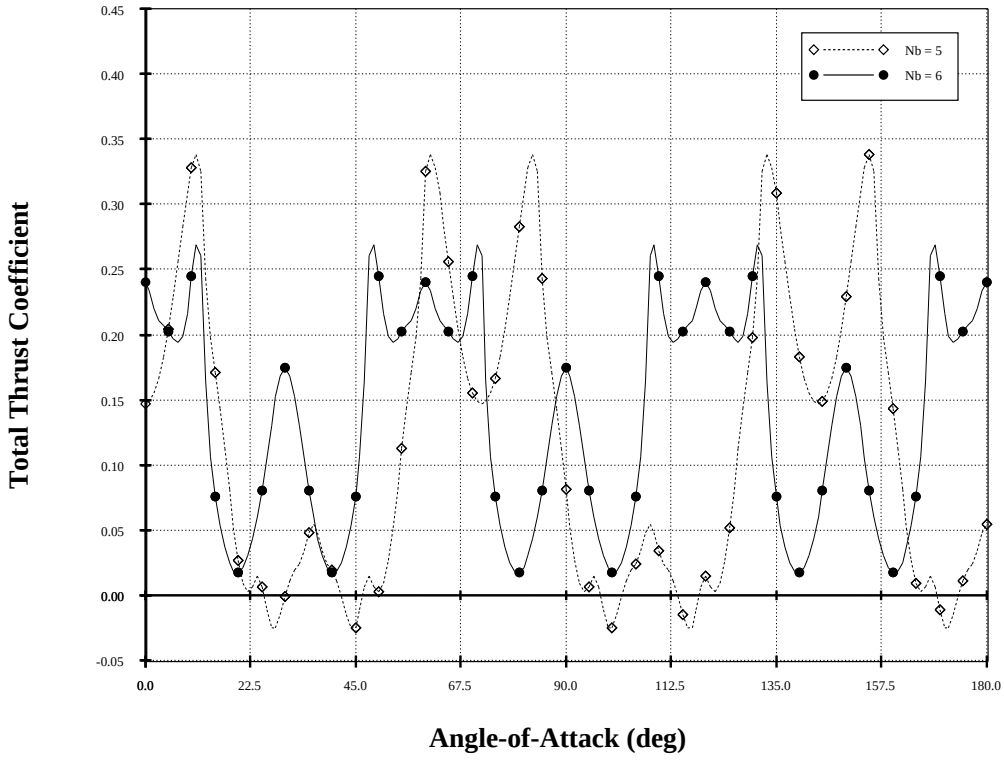

Figure 8: Start-Up Thrust Coefficients using 5 & 6 Blades.

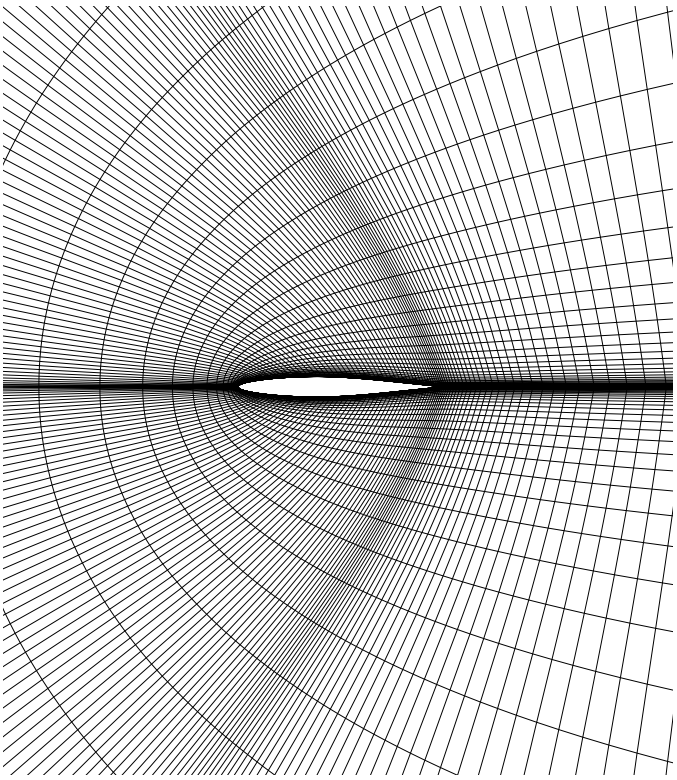

Figure 9: C-mesh with Viscous Clustering about a NACA64A010 Airfoil.

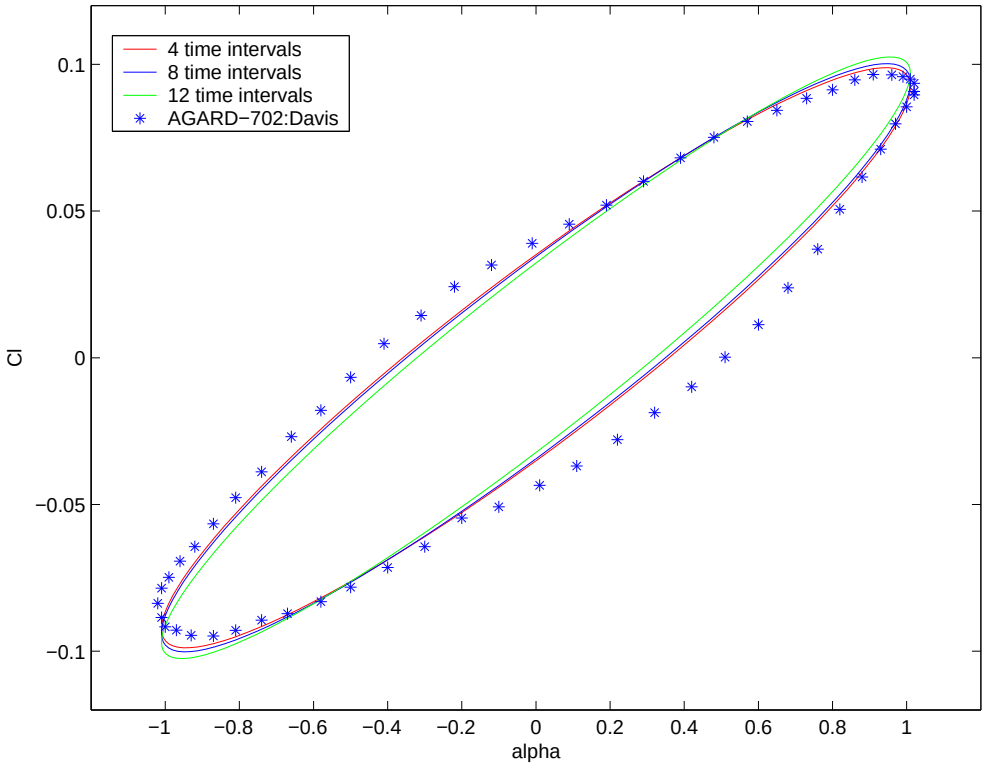

Figure 10: NACA64A010 Dynamic Lift Loop.

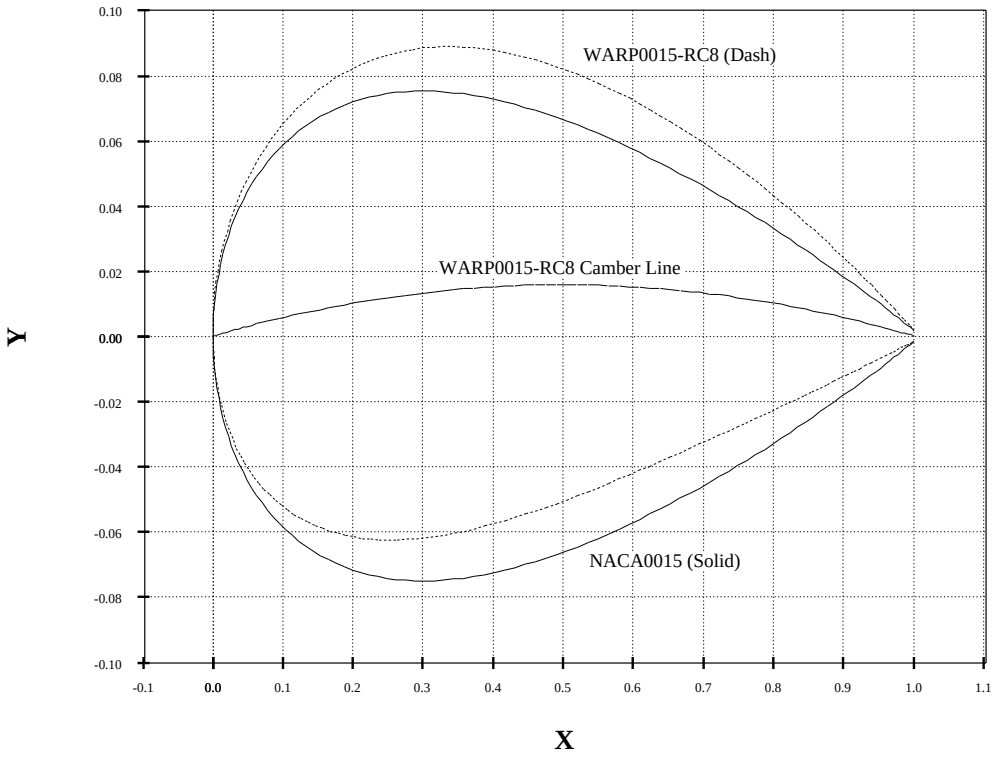

Figure 11: Comparison of NACA0015 & WARP0015-RC8 Airfoil Sections.

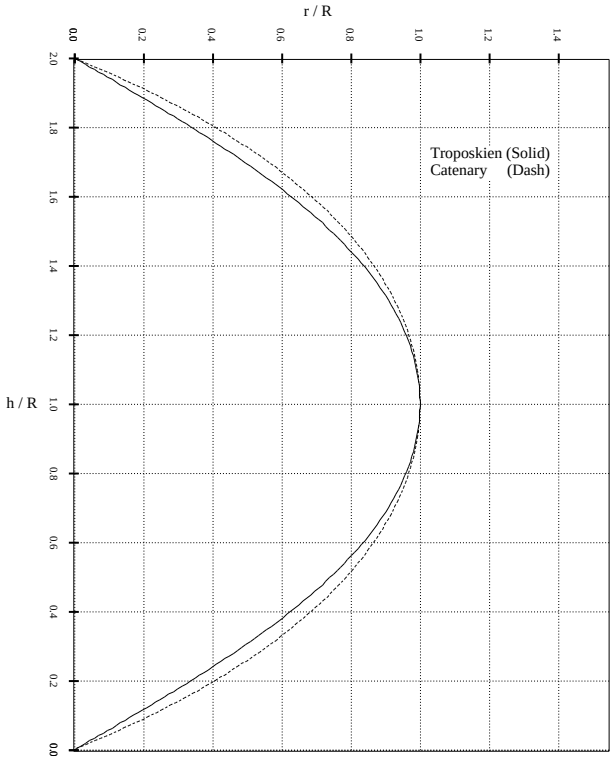

Figure 12: Comparison of Troposkien & Catenary Curves.

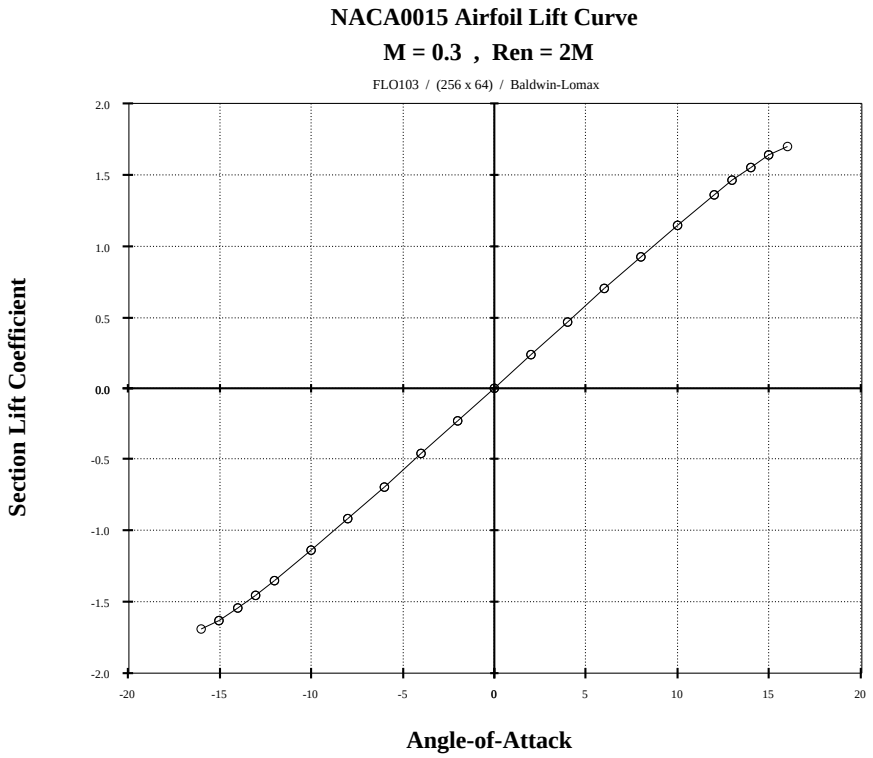

Figure 13: FLO103 Computed C_l-α Curve.

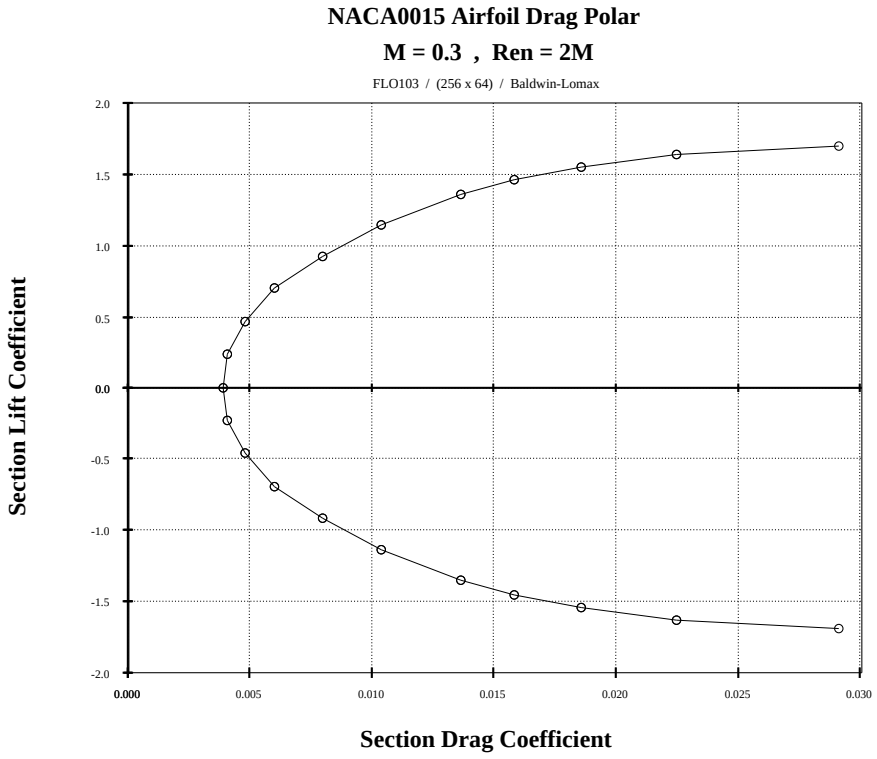

Figure 14: FLO103 Computed Drag Polar.

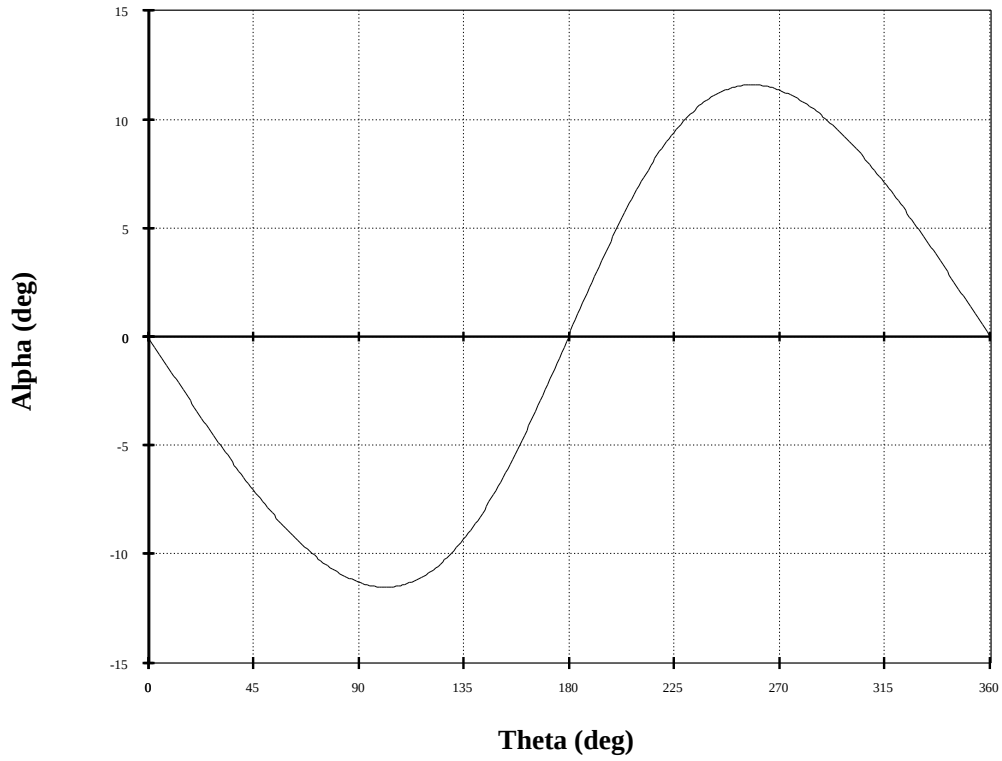

Figure 15: Geometric Angle-of-Attack Variation for $\chi = 5.0$.

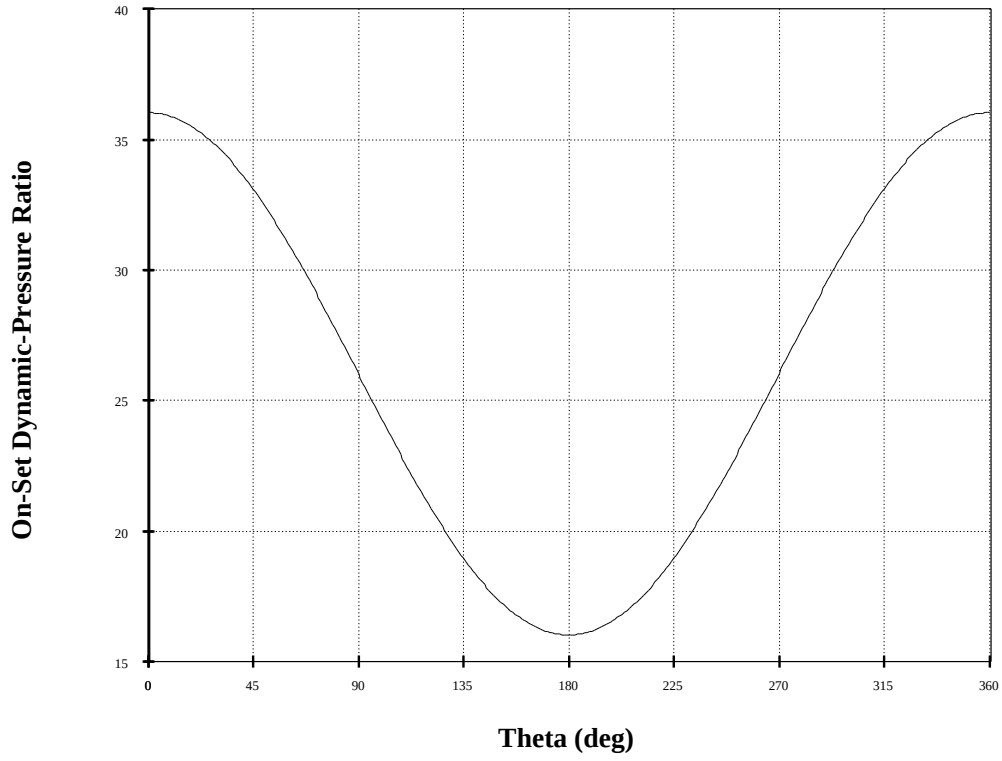

Figure 16: On-Set Dynamic Pressure Ratio Variation for $\chi = 5.0$.

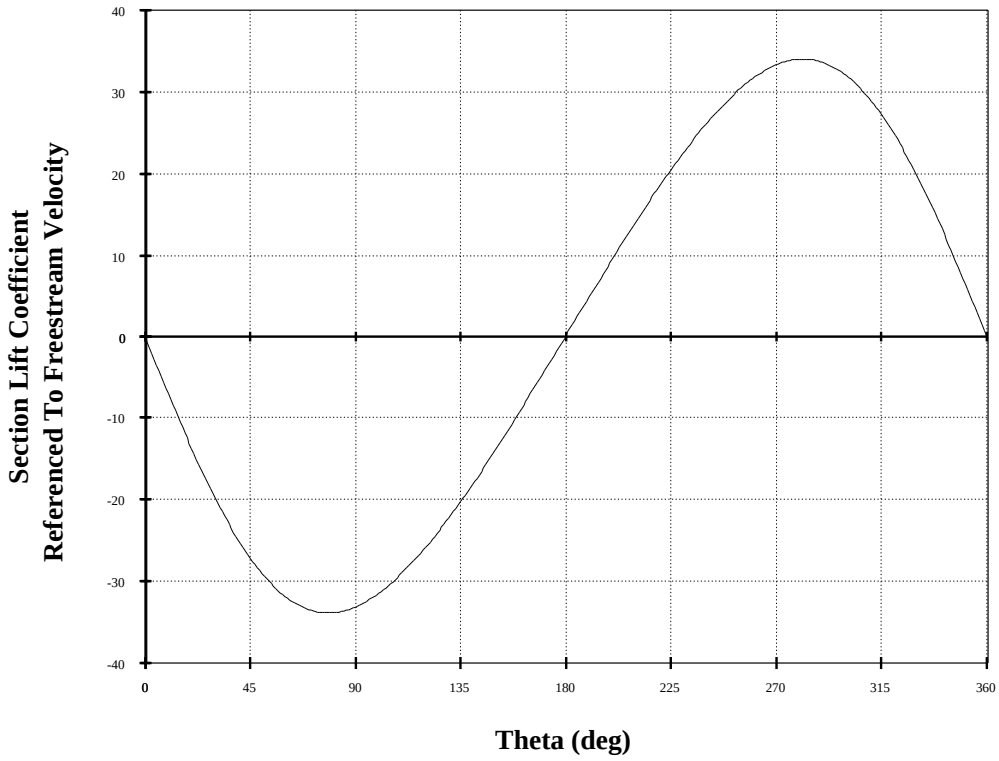

Figure 17: Variation of Lift for $\chi = 5.0$.

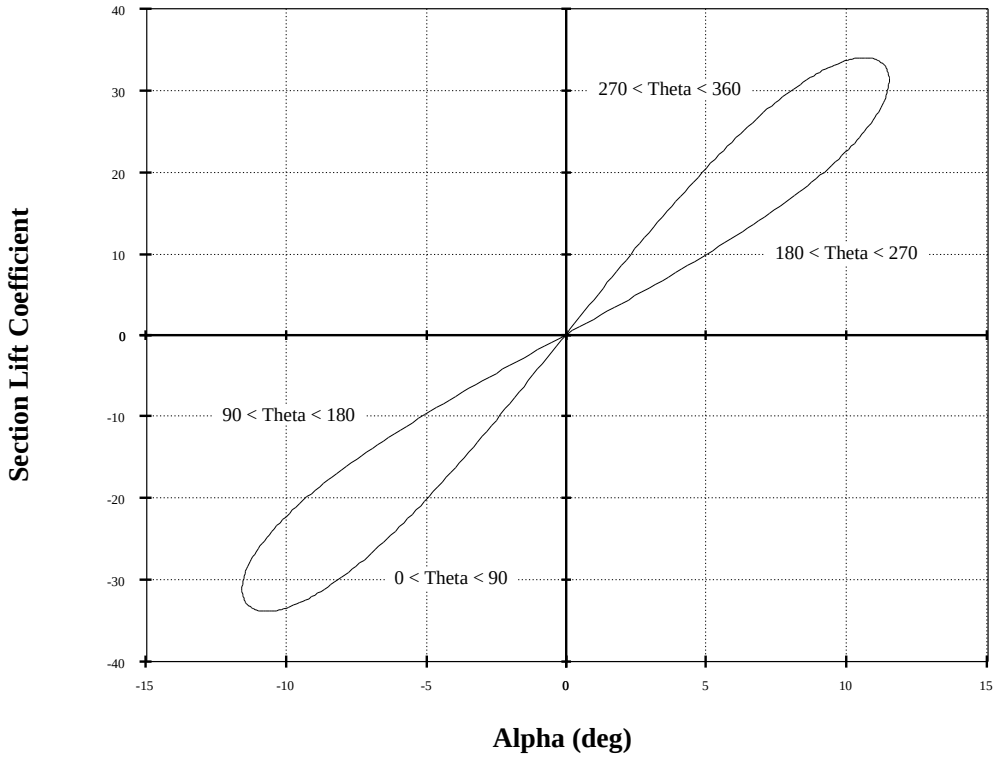

Figure 18: Lift Loop for $\chi = 5.0$.

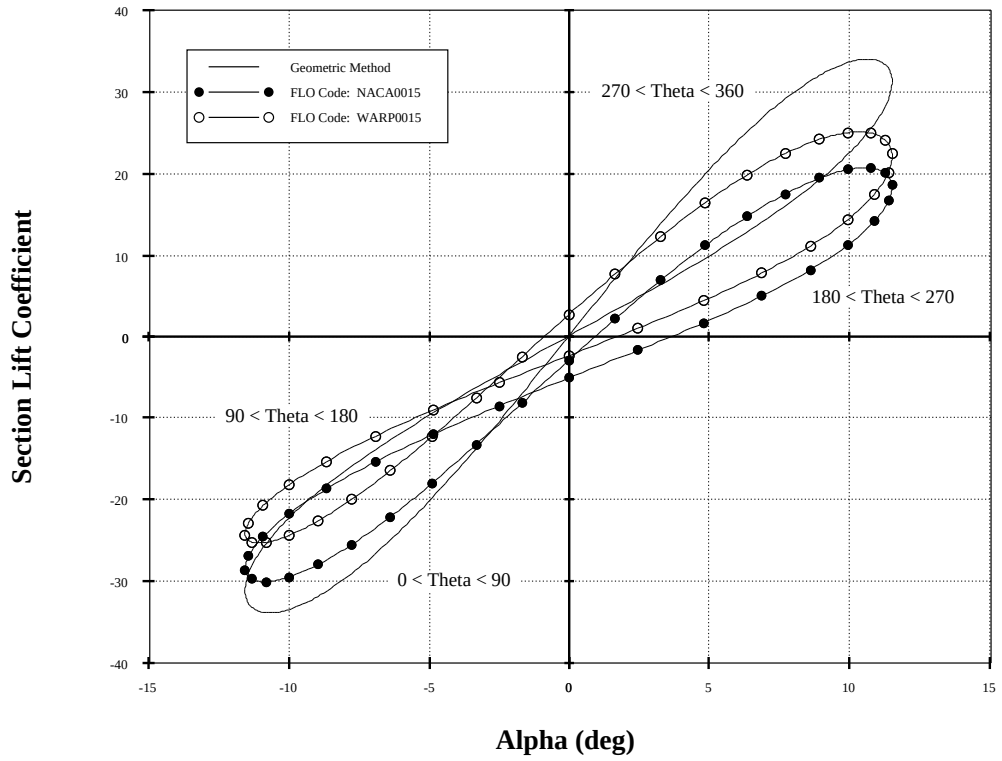

Figure 19: Comparison of Symmetry-Plane Sectional Lift Loops for $\chi = 5.0$.

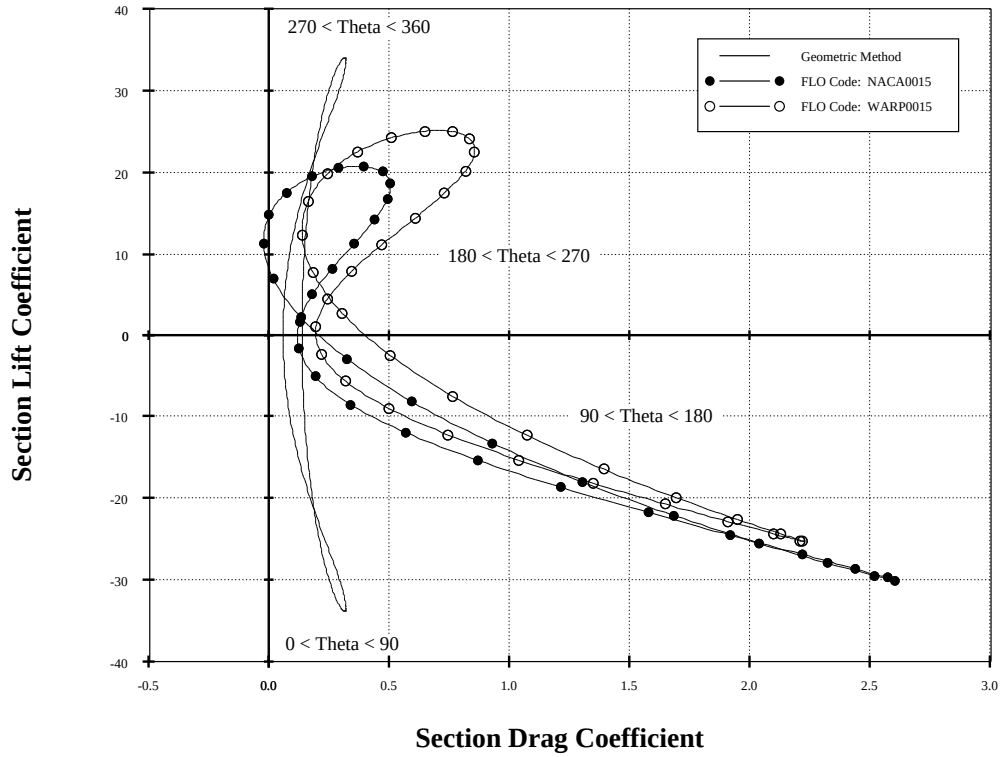

Figure 20: Comparison of Symmetry-Plane Sectional Drag-Polar Loops for $\chi = 5.0$.

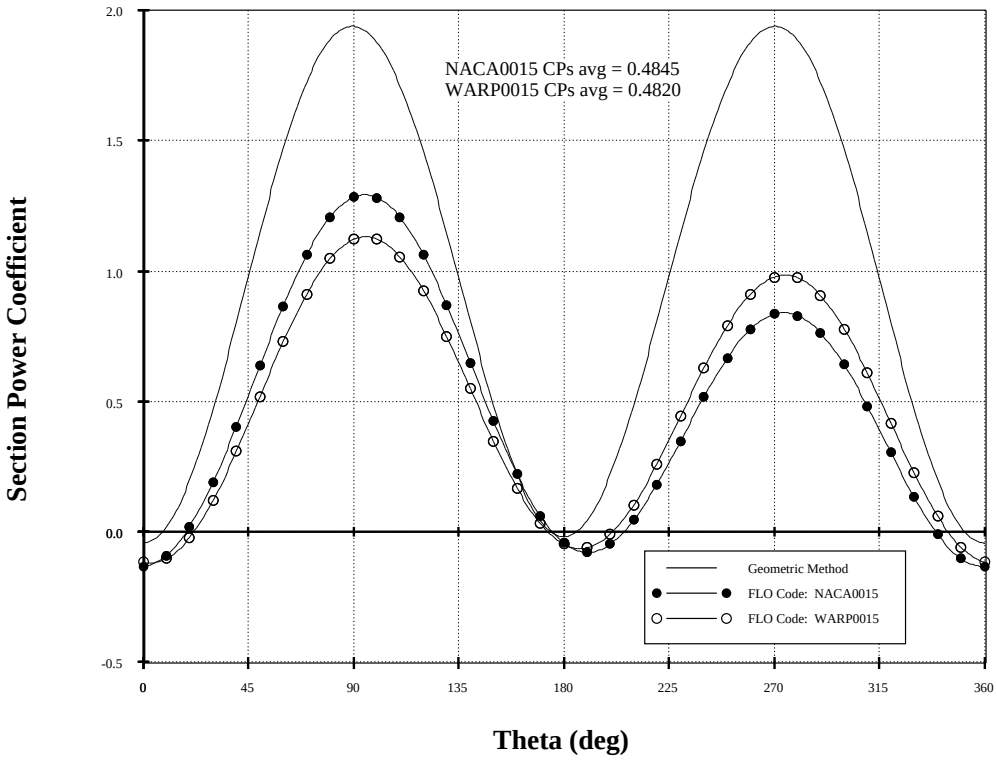

Figure 21: Comparison of Symmetry-Plane Sectional Power Cycles for $\chi = 5.0$.

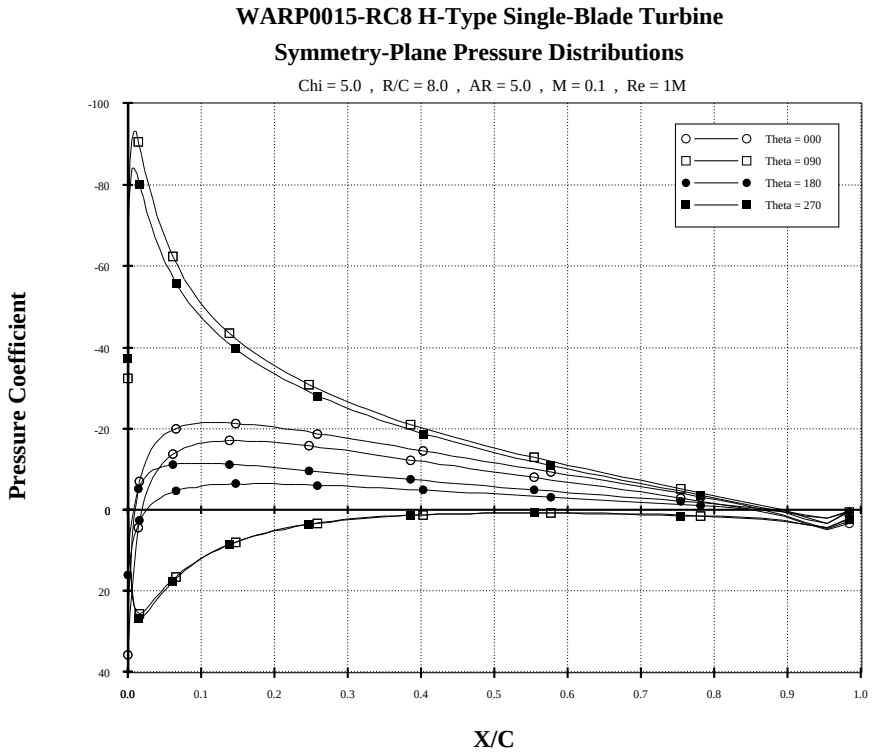

Figure 22: Symmetry-Plane Pressure Distributions for $\chi = 5.0$ at Various Clock Positions.

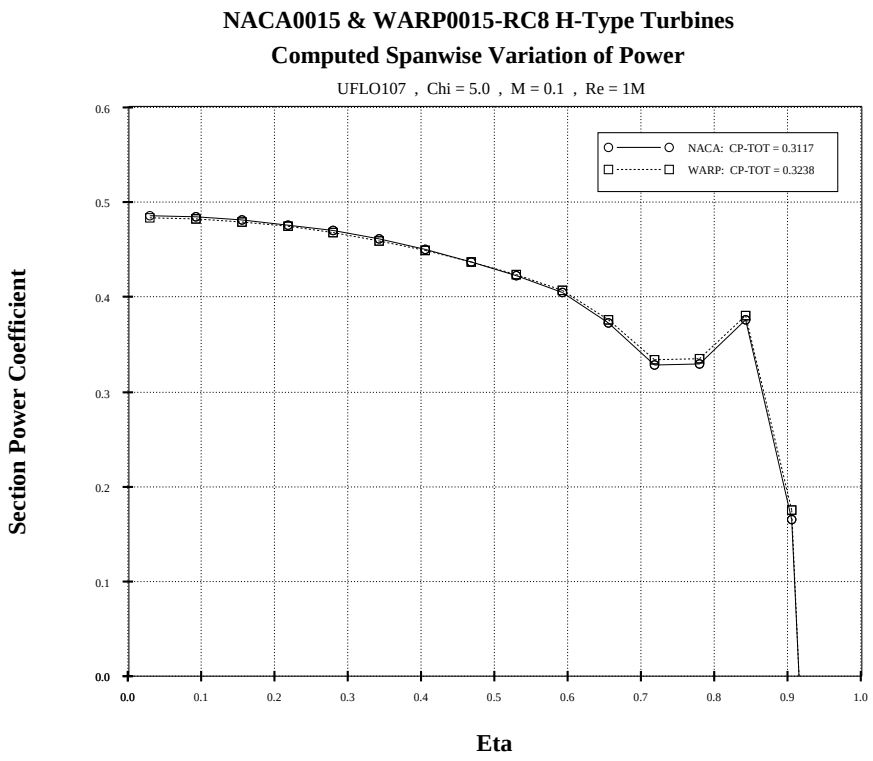

Figure 23: Computed Spanloads of the NACA0015 & WARP0015-RC8 H-Type Turbines at $\chi = 5.0$.

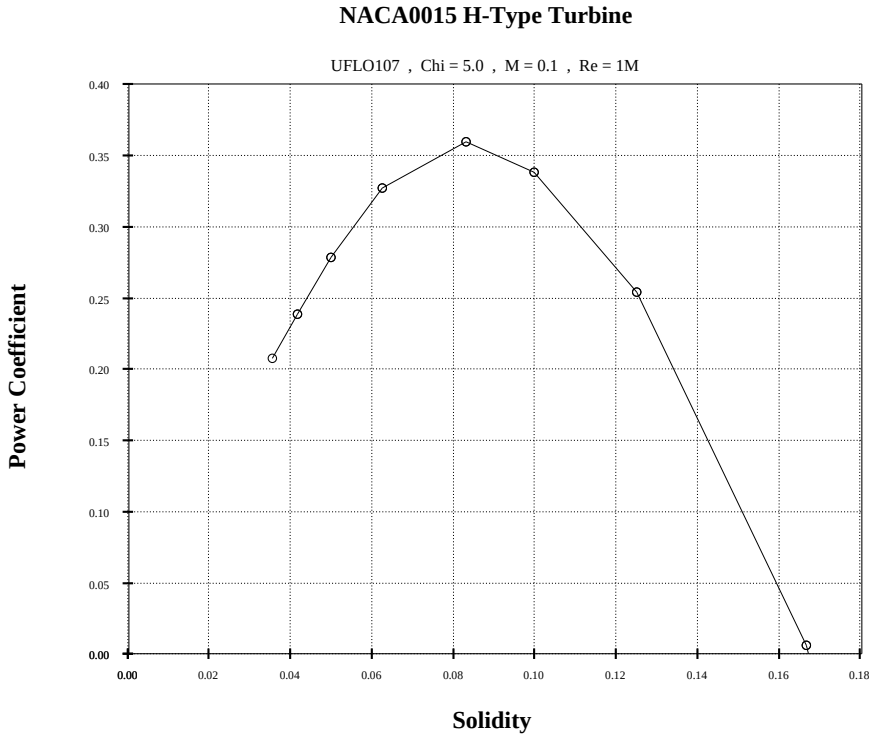

Figure 24: Effect of Solidity on Power Coefficient for the NACA0015 H-Type Turbine at $\chi = 5.0$.

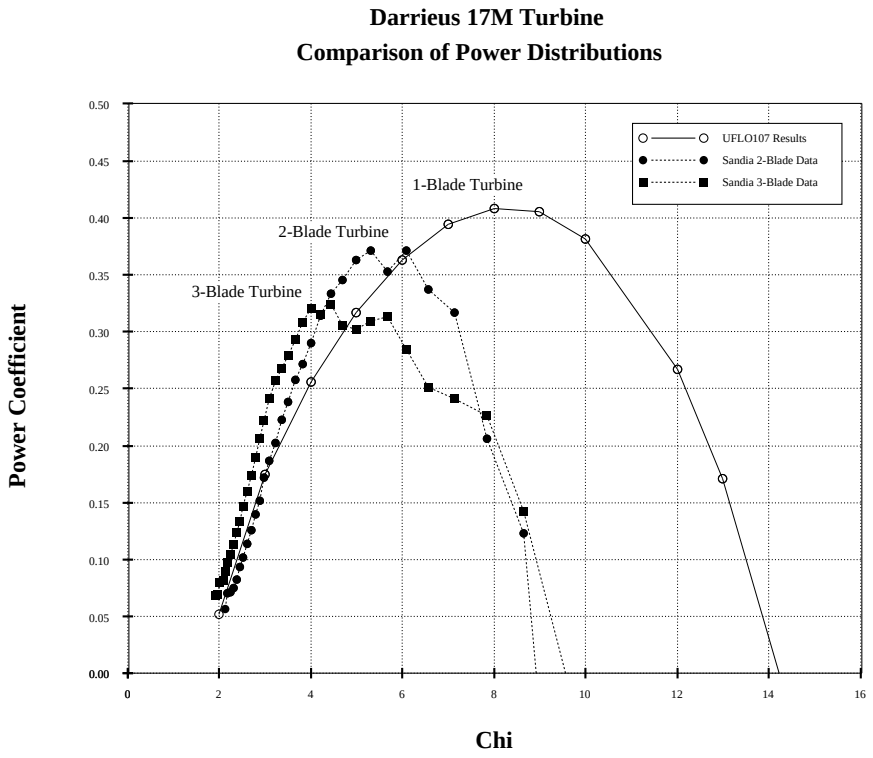

Figure 25: Comparison of Darrieus 17M Power Distributions.

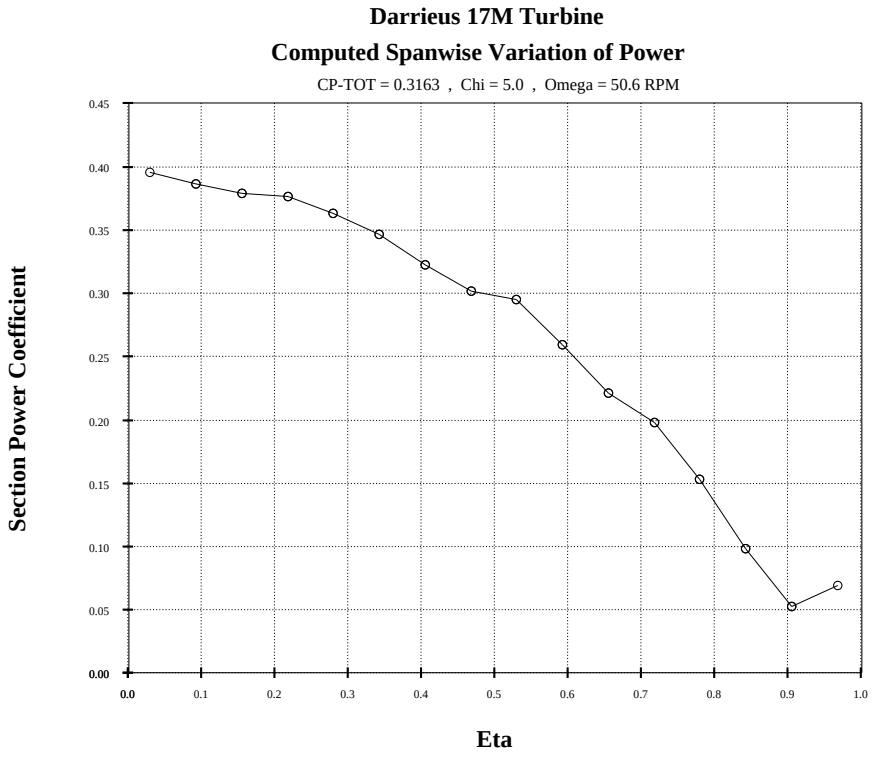

Figure 26: Computed Spanload of the Darrieus 17M Turbine at $\chi = 5.0$.

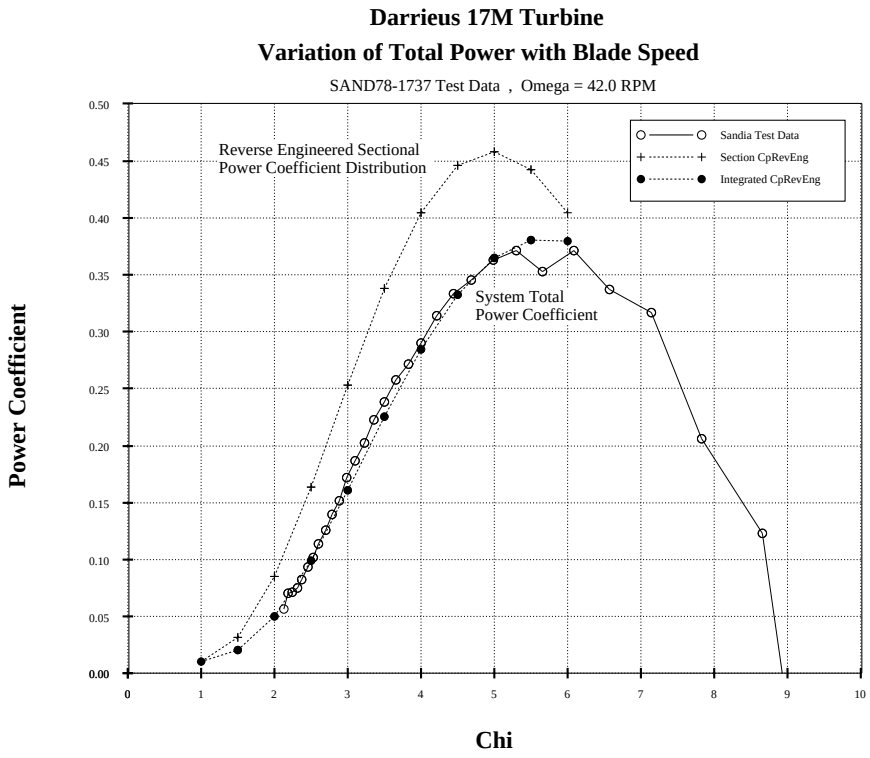

Figure 27: Reversed Engineered Sectional Power Coefficients from System Total Distribution.

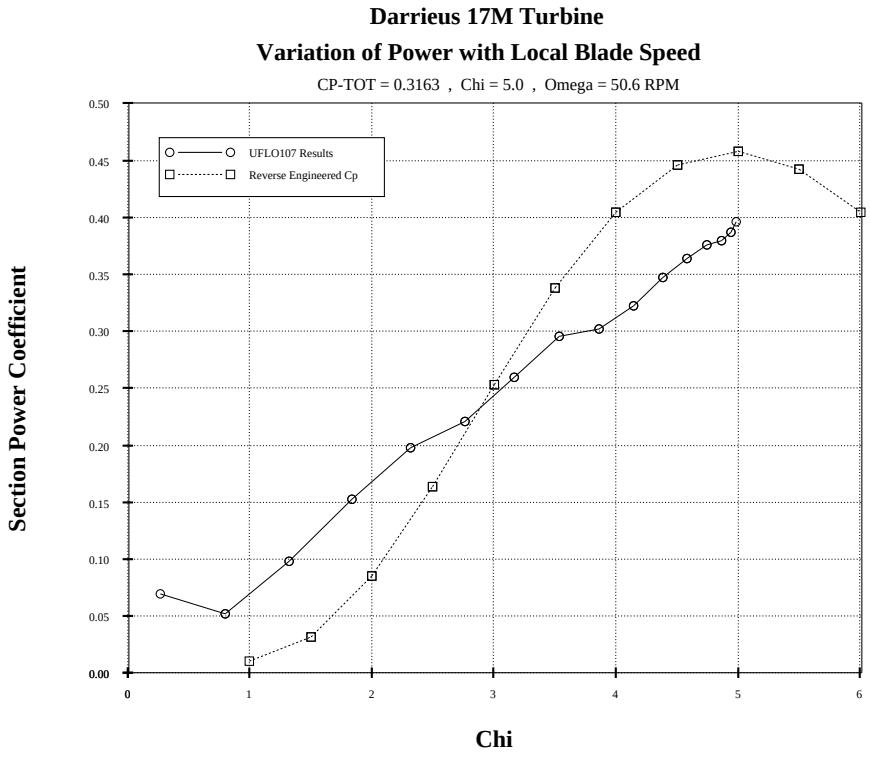

Figure 28: Comparison of Sectional Power Coefficient Distributions for Darrieus 17M at $\chi = 5.0$.